Realistic simulations of atmospheric gravity waves over the continental US using precipitation radar data

Claudia Stephan,[1] and M. Joan Alexander,[2]

Corresponding author: Claudia Stephan, Department of Atmospheric and Oceanic Sciences, 311 UCB, Folsom Stadium, Rm 255, University of Colorado, Boulder, CO 80309, USA. (a.b.claudia.stephan@colorado.edu)

[1]Department of Atmospheric and Oceanic Sciences, University of Colorado, Boulder, Colorado, USA

[2]NorthWest Research Associates, Inc., CoRA Office, Boulder, Colorado, USA

Abstract. Convectively-forced gravity waves can affect the dynamics of the upper troposphere and middle atmosphere on local to global scales. Simulating these waves requires cloud-resolving models, which are computationally expensive and therefore limited to case studies. Furthermore, full-physics models cannot accurately reproduce the locations, timing, and intensity of individual convective rain cells, limiting the validation of simulated waves. Here, we present a new modeling approach that retains the spatial scope of larger scale models but permits direct validation of the modeled waves with individual cases of observed waves. Full-physics clouds-resolving model simulations are used to develop an algorithm for converting instantaneous radar precipitation rates over the US into a high-resolution latent heating/cooling field. This heating field is used to force an idealized dry version of the WRF model. Wave patterns and amplitudes observed in individual satellite overpasses are reproduced with remarkable quantitative agreement. The relative simplicity of the new model permits longer simulations with much larger and deeper domains needed to simulate wave horizontal/vertical propagation. Eliminating the complicating factors of cloud physics and radiation this approach provides a link between conceptual and full-physics models and is suitable for studying wave-driven far-field circulation patterns.

1. Introduction

Recent studies have emphasized the stratosphere's role in affecting surface weather and climate. *Charlton et al.* [2004] highlight the sensitivity of medium-range tropospheric forecast skill to the stratospheric initial state. Focusing on the southern hemisphere, *Roff et al.* [2011] suggest that an increased model stratospheric resolution with an improved representation of stratospheric dynamics and thermodynamics improved the quality of extended-range forecasts. *Scaife et al.* [2011] show that stratosphere-troposphere interactions change climatological predictions for the Atlantic storm track with substantial impact on extreme winter rainfall over Europe. As a consequence, models used for operational forecasting, seasonal prediction, and coupled climate simulations are raising their tops to include more stratospheric processes including nonorographic gravity wave drag [*Pawson et al.*, 2000; *Manzini et al.*, 2014]. Clarifying the degree to which small scale gravity waves need to be represented in weather prediction and climate models remains an important and active area of research (e.g. *Schirber et al.* [2014]).

Convection is known to be an important source of gravity waves, especially in the tropics and summer midlatitudes. Cloud-resolving numerical models now include a multitude of interactive physics packages that can be customized to yield accurate simulations of sub-cloud scale processes. Numerous studies have successfully used such models to relate convective properties to the generated gravity wave spectrum [*Alexander and Holton*, 1997; *Piani et al.*, 2000; *Lane et al.*, 2001; *Song et al.*, 2003; *Beres*, 2004; *Choi and Chun*, 2011]. These results have guided the development of source parameterizations for GCMs that deliver a momentum-flux spectrum that depends on the latent heating properties of

the underlying convection and the background wind [*Beres et al.*, 2004, 2005; *Chun and Baik*, 2002; *Kim et al.*, 2013]. While a realistic representation of the general circulation can be achieved with these parameterizations, they make assumptions that can lead to inaccuracies, particularly in local and regional circulations. Common assumptions include that waves propagate, within one time step, and within the same column, to the heights where they deposit their momentum and create drag. It has been pointed out that these assumptions are not consistent with general propagation properties of gravity waves and do not necessarily ensure physically consistent wave-induced forcing [*Song and Chun*, 2008; *Sato et al.*, 2009, 2012].

Here, we present a new modeling approach that permits direct validation with satellite overpass measurements of waves above storms. Cloud resolving models with full physics cannot accurately predict the locations, timing, and intensity of individual convective rain cells that are the important sources of the waves. Our approach forces an idealized dry version of the WRF model with high-resolution latent heating/cooling derived from precipitation observations over the continental US. Instantaneous radar rain rates are converted to latent heating/cooling with an algorithm trained using full-physics clouds-resolving model (CRM) simulations. Unlike CRM simulations the new model not only permits direct validation with satellite data, it also permits much larger and deeper domains needed to simulate wave horizontal/vertical propagation and driving of the far-field circulation. The idealized framework also provides a link between conceptual and full-physics models, permitting clearer interpretations of wave-driven circulations without the complicating factors of cloud physics and radiation [*Hoskins*, 1983].

The approach is similar to *Grimsdell et al.* [2010], but the use of CRMs to train the algorithm is new, and the results give excellent quantitative comparisons to observed waves. Recent work [*Stephan and Alexander*, 2014] has shown that the simulated gravity wave spectrum is fairly insensitive to the physics parameterization choices used in WRF. This permits us to therefore focus on a single set of physics parameterizations that gives the best representation of storm morphologies to train our heating/cooling algorithm. The effectiveness of this new approach is proven here by comparing modeled waves to observations above several different storm types with remarkable success.

The Advanced Research WRF (ARW) model is able to simulate cloud-scale processes for both simplified, idealized frameworks and full-physics runs initialized with assimilated observations. We will refer to these as "idealized" and "full-physics" runs, respectively. In section 2 we introduce the setup of two full-physics storm simulations, a squall line and a mesoscale convective complex (MCC). The algorithm for obtaining vertical heating/cooling profiles from local precipitation rates is derived from the full-physics squall line simulation in section 3. Section 4 contains a description of the idealized model, followed by a comparison between the full-physics and idealized model simulations of the squall line and MCC case. In this comparison it is shown that the spectrum of waves in the full-physics model is reproduced in the idealized model, when forced with the respective precipitation-derived heating rates. In section 5 we apply our heating/cooling algorithm to precipitation radar observations and force idealized model simulations with these radar-derived heating rates. These simulations are run with large areas and deep domains in order to compare the simulated waves to instantaneous satellite observations

of gravity waves above three different storm cases for validation of the new model method. Section 6 is a discussion and conclusion.

2. Full-physics simulations

Full-physics simulations use reanalysis products to define three-dimensional wind, pressure, temperature and humidity fields as well as time-sensitive land-surface fields (snow-cover, soil temperature, soil moisture) for initial and boundary conditions. They are typically run with a combination of physics packages including microphysics, cumulus parameterization, surface physics, planetary boundary layer and atmospheric radiation schemes. Idealized experiments allow for simplified physics and user-defined initial conditions, which reduces their runtime significantly.

Both the full-physics and the idealized model are nonlinear and non-hydrostatic, and use a Runge-Kutta 3rd-order time integration scheme with 5th-order horizontal momentum and scalar advection and 3rd-order vertical momentum and scalar advection. These odd-order schemes have some inherent diffusivity (see *Skamarock* [2008] for further details on the model equations). In addition we are using explicit 6th-order hyperdiffusion in both the full-physics and idealized simulations. The application of this scheme in WRF is discussed in *Knievel et al.* [2007].

Modeling a summer-time squall line on 5 June 2005 over the Great Plains, *Stephan and Alexander* [2014] investigated the impact of the choice of physics parameterizations on gravity wave generation. The shape and magnitude of the simulated stratospheric gravity wave momentum flux spectra did not critically depend on the microphysics scheme. For the full physics storm simulations in this study we use the same combination of physics schemes as the MOR1 simulation of *Stephan and Alexander* [2014], which in a comparison

with radar measurements was found to accurately reproduce the storm structure. The Kain-Fritsch [*Kain and Fritsch*, 1990] cumulus scheme is only active on the 18 km domain. On the 6 km and 2 km domains precipitation processes are handled by the Morrison microphysics scheme [*Morrison et al.*, 2009]. The remaining physics choices are the Yonsei University planetary boundary layer scheme [*Hong et al.*, 2006], the Goddard scheme [*Chou and Suarez*, 1999] for short-wave radiation, the Rapid Radiative Transfer Model [*Mlawer et al.*, 1997] for long-wave radiation and the Noah Land Surface Model [*Ek at al.*, 2003].

Three nested domains with horizontal resolutions of 18 km, 6 km and 2 km are connected through a one-way nesting procedure. We choose 2 km to match the resolution of our idealized runs described in section 4. This resolution is also sufficient for satellite validation and produces results of very similar quality as the 1-km-resolution model used in *Stephan and Alexander* [2014] when validated against radar precipitation fields.

Figure 1 shows ten-minute precipitation rates over the inner domain at 0200, 0400, 0600 and 0800 UTC. Precipitation radar measurements (left column) are contrasted with model output (right column). The inner domain spans 600 km×600 km and is initialized at 1800 UTC on 4 June 2005. Fig. 1 shows that the period 0100 UTC to 0800 UTC contains fully developed to decaying storm stages and accordingly encompasses a large variety of precipitation strength distributions. Therefore, this seven-hour period provides a range of conditions suitable for deriving an algorithm that may be more universally applicable to continental US severe storm systems.

The outer domain is initialized with ERA-interim (European Centre for Medium-Range Weather Forecasting Re-Analysis) data [*Dee at al.*, 2011], which is available at six-hour

intervals at a nominal resolution of 0.7°. The vertical grid, consisting of 95 terrain-following levels, is stretched between the surface and 850 hPa and beyond this point has a constant spacing of about 250 m. A 5-km deep Rayleigh damping layer that was previously shown [*Stephan and Alexander*, 2014] to prevent unphysical wave reflection at the upper boundary is placed below the model top of 40 hPa (22 km).

The second storm we simulate with the full-physics model is a mesoscale convective complex, which occurred on 20 June 2007 over the Great Plains. The area of the inner model domain for the MCC simulation is four times larger than for the squall line case and spans 1200 km ×1200 km. This second case is used to confirm that algorithm and model perform well in other scenarios. This storm is chosen because it has multiple characteristics that distinguish it from the squall line event. Fig. 2 shows the simulated (right column) and radar (left column) precipitation field at a 4 km ×4 km horizontal resolution over the inner model domain. Comparing to Fig. 1 the MCC exhibits a more oval structure in the horizontal in contrast to the narrow linear shape of the squall line. The MCC is in a mature developmental stage throughout the 0100 UTC to 0800 UTC time interval and consists of a larger connected area of convection. The full-physics MCC simulation uses identical physics and diffusion settings as the squall line simulation.

3. Heating algorithm

In this section we develop an algorithm that relates precipitation rate to a profile of latent heating for severe storm conditions. To derive the heating algorithm we use the innermost domain of the full-physics squall line simulation, where moist processes are exclusively governed by a microphysics (MP) scheme. The microphysics latent heating/cooling

enters the model through the thermodynamic equation

$$\partial_t(\mu\theta) + (\nabla \cdot \mu\mathbf{v}\theta) = F_\theta. \quad (1)$$

Here, θ denotes the potential temperature, $\mu(x, y)$ is the mass per unit area within a column in the model domain at (x, y), $\mathbf{v}$ is the three-dimensional velocity vector and

$$F_\theta = F_{\theta,MP} + F_{\theta,rad} + F_{\theta,cum} + F_{\theta,pbl} + F_{\theta,mix/dif} \quad (2)$$

represent potential temperature tendencies arising from microphysics, radiation, cumulus parameterization, planetary boundary layer schemes, mixing and diffusion. To ensure correct saturation conditions the microphysics tendency $F_{\theta,MP}$ is evaluated at the end of each time step and stored in a variable called *h_diabatic*. We use this field to find a relationship between ten-minute precipitation rates and characteristics of the vertical heating/cooling profile. Ten minutes is chosen to match nominal radar observation intervals used later in this study. The heating algorithm is developed at a horizontal resolution of 4 km $\times$4 km, also to match the resolution of the radar data.

Figure 3 a shows the simulated latent heating/cooling profiles averaged over the convective pixels in the inner domain as a function of ten-minute precipitation rate and height. We only apply the algorithm to grid points that exceed a precipitation threshold of 1.0 mm(10 minutes)$^{-1}$, chosen as the smallest integer value for which the binned peak heating amplitudes exceed 0.004 K/s. This value is typical for heating rates observed in squall lines [*Chong and Hauser*, 1990; *Braun and Houze*, 1996], and was found to provide a useful definition of a convective pixel in *Stephan and Alexander* [2014].

Key characteristics of these profiles and their dependence on the precipitation rate are examined in Fig. 4. Both figures 3 and 4 use the same precipitation bins, which are

chosen such that each bin contains 400 members. From Fig. 3 it is evident that there exists a broad elevated heating region with a subjacent shallow cooling layer, which likely represents the cold pool [*Rotunno et al.*, 1988; *Moncrieff*, 1992; *Morrison and Milbrandt*, 2011]. The orange data points in Fig. 4 depict the height where the positive heating peak is reached. We define the top of the heating (light green) as the location where the heating rate falls to 10% of its maximum and the bottom of the heating profile (purple) as the height where the heating rate approaches zero. The green, yellow and blue points at the bottom of Fig. 4 show the top of the cooling region, defined as the height where the profile turns from negative to positive values, the height of the cooling peak, and the bottom of the cooling region, respectively. The straight lines through these six sets of points are linear fits. The corresponding equations are used to convert precipitation rates in units of mm(10 minutes)$^{-1}$ to height in units of kilometers and are listed in Fig. 4. The remaining two linear fits (dark red) pertain to the ordinate on the right-hand side of Fig. 4 and show the heating and cooling amplitude as a function of ten-minute precipitation rate.

In assigning the full vertical heating/cooling profile we assume a quarter-sine shape for each of the four sections, i.e. top of heating to peak of heating, peak of heating to bottom of heating, top of cooling to peak of cooling and peak of cooling to bottom of cooling. When applied to the simulated precipitation field this method accurately reproduces the shape of the heating distribution (Fig. 3 b). The superimposed histograms compare the density-weighted vertically integrated heating rates, labeled Q, computed from the algorithm-generated profiles with those from the simulations. Q should be directly related to the net amount of condensation/evaporation in the column. The similarity of the two histograms therefore affirms that our technique yields consistent results.

Since we used numerical data over a period of seven hours it is not obvious that the established relationship between ten-minute precipitation rate and column heating is valid for each stage of the storm. Fig. 5 compares the simulated (solid) and the algorithm-produced (dashed) vertical heating profiles every ten minutes where colors indicate different times. Each profile is the domain average of columns with precipitation rates greater than 1 mm(10 minutes)$^{-1}$. This plot reveals that the algorithm outlined in this section captures the time-evolution of the heating field nearly perfectly, which is important to achieve a realistic representation of wave intermittency in the simulations.

4. Idealized model

4.1. Idealized model setup

In the idealized model the cumulus, microphysics, radiation, surface and planetary boundary schemes are turned off, which makes the model computationally efficient without jeopardizing the realistic representation of gravity wave propagation and dissipation.

In the full-physics runs during the third-order Runge-Kutta (RK3) time stepping, all forcing terms in Eq. 2 except for the microphysics tendency are computed during the first RK3 sub-step and are held constant throughout the remaining two sub-steps. High-frequency acoustic modes are integrated during small-step loops embedded in the RK3 large-time-step sequence. To avoid the excitation of unwanted acoustic waves it is necessary to incorporate an estimate of the MP tendency. For this purpose, the full-physics version of WRF stores the MP latent heating/cooling rate from the previous step in the variable *h_diabatic*. This tendency is included in the acoustic loop of the subsequent time step and then removed from the temperature field at the end of the last acoustic time step. Finally, the MP scheme is called to update $F_{\theta,MP}$ with the correct tendency.

In our modified version of the idealized model the MP scheme is turned off and the latent heating field is instead imported from an auxiliary file. It is read in as the variable *h_diabatic* and takes the place of the MP tendency estimate. Consequently, it is added to the temperature field for the acoustic integration. We modified the source code such that this estimate is no longer removed at the end of the acoustic integration but remains as $F_{\theta,MP}$ forcing the potential temperature field.

As in the full-physics model, vertical levels are specified in terms of a terrain-following hydrostatic-pressure vertical coordinate $\eta = (p_h - p_{ht}) / (p_{hs} - p_{ht})$, where p_h denotes the hydrostatic component of pressure, p_{ht} the pressure at the model top, and p_{hs} the pressure at the surface. For the purpose of validating the idealized model, in this section we specify the η levels, model top pressure and damping layer properties of the idealized model to be identical to the full-physics simulations described in section 2. Given that there exists no topography in the idealized simulations, p_{hs} is constant and η-levels coincide with base-state geopotential levels. For the comparison with the full-physics squall line and MCC simulations the horizontal grid dimension in the idealized runs are also chosen to be identical to the respective full-physics simulations. To attain a smooth time variation we interpolate the heating field from ten-minute to two-minute time intervals before storing it in the auxiliary WRF heating input file.

There is no moisture in the idealized model. The idealized model is initialized with a dry sounding of wind and potential temperature. In this section we use the domain-mean 0100 UTC wind and temperature fields of the respective full-physics simulation to compute the sounding. Figure 6 shows the resulting profiles of zonal and meridional velocity and

potential temperature for the squall line case (left) and the mesoscale convective complex (right).

4.2. Idealized model validation

To evaluate the performance of the idealized model we first apply the heating algorithm to the simulated precipitation fields of the squall line and MCC simulations, force the model with this algorithm-derived heating, and compare the resulting dynamics in the idealized model to the corresponding full-physics simulations. The idealized simulations are compared with their full-physics counterparts over the time period 0100 UTC to 0800 UTC. The idealized simulations are initiated at 0000 UTC to allow for one hour of spin-up time.

The heating algorithm derived in section 3 is based on the full-physics WRF simulation of a squall line event. To validate the idealized model we first apply the algorithm to the precipitation field from this simulation and compare the vertical velocity spectra and gravity momentum flux spectra of the full-physics and the idealized simulation. To test if algorithm and model perform well in other scenarios we repeat the analysis for the mesoscale convective complex (MCC) simulation.

4.2.1. Squall line case

The left two panels of Fig. 7 show the gravity wave momentum flux spectra at 95 hPa for the full-physics and the idealized squall line simulations as a function of phase speed (radial coordinate) and propagation angle. These spectra are obtained from seven hours of data at 2 min time resolution and represent averages over an area of 576 km $\times$576 km. For further details on the computation of the spectra see *Stephan and Alexander* [2014]. The idealized model successfully replicates the general shape of the full-physics

model spectrum and the total flux is within 12%. The roughly circular regions of low values that appear in the northeast quadrants of the momentum flux spectra are caused by wind filtering between the top of the heating region and 95 hPa. This occurs when a wave approaches a level where the phase speed equals the wind speed. As is evident from Fig. 6 there exists strong shear at these levels in both the zonal and meridional direction.

Figure 8 displays the power spectral density as a function of zonal wavenumber for the zonal, meridional and vertical velocity components at 95 hPa and 0500 UTC. Each line represents a latitudinal average at a single time step. The dashed curves of the idealized model show remarkable agreement with the solid curves of the full-physics model. The spectra of both models start to decay around $4{\cdot}10^{-4}\mathrm{m}^{-1}$, which corresponds to a horizontal wavelength of about 16 km, or 8 times the grid scale, which is consistent with the WRF model's effective resolution of about $7\Delta x$ [*Skamarock*, 2004].

4.2.2. Mesoscale convective complex

The two spectra on the right of Fig. 7 show the gravity wave momentum flux spectra at 95 hPa produced by the full-physics and the idealized MCC simulations. Both spectra feature a large peak of gravity wave momentum flux in the westward direction and a smaller second peak in the southeastward direction. Compared to the squall line spectra the hole created by wind filtering is slightly smaller and more north-south symmetric. The shape of the spectrum is again accurately reproduced by the idealized model and the magnitude of the flux is 20% larger than in the full-physics simulation. Although this storm differs considerably from the squall line case, the heating algorithm is apparently still applicable, so that in many respects the quality of the results remains unaffected.

4.3. Simulations based on radar data

In order to apply the heating algorithm to ten-minute radar precipitation fields (e.g. left columns of Fig. 1 and Fig. 2), we obtain the Storm Total Rainfall Accumulation Product (STP) for individual Next-Generation Radar (NEXRAD) stations. The STP product provides radar-estimated rainfall accumulations within 230 km of the radar in polar coordinates with a resolution of 2 km $\times 1^\circ$. Data from several stations are interpolated in space and time to obtain a ten-minute 4 km $\times$4 km mosaic. In this process we average overlapping arrays from different stations to obtain smooth maps. Model setup and domain sizes are identical to the corresponding runs in the previous section.

Fig. 9 shows the gravity wave momentum flux spectra at 95 hPa for the idealized simulations forced with heating derived from radar precipitation. For both the squall line and the MCC case the resulting spectra compare well to the respective full-physics WRF simulations (Fig. 7). For the squall line case the integrated momentum flux of the spectrum based on radar precipitation is 23% larger than in the full-physics WRF simulation which is consistent with a 22% larger domain-mean and time-mean precipitation in the observations. For the MCC the full-physics and radar-based domain-mean precipitation amounts averaged over the seven-hour time interval differ by only 1%. The 68% larger flux in the radar-based simulation might be associated with more intense rain cells. (See Fig. 2.)

5. Comparison with satellite measurements

Up to this point we have examined gravity waves only in model simulations. In this section we present a direct comparison of simulated stratospheric gravity waves to satellite observations for three different storms, the familiar squall line and MCC cases and a

mesoscale convective system (MCS) that occurred on 13 June 2013 over the northeastern US.

The Aqua satellite is part of the National Aeronautics and Space Administration's Earth Observing System A-Train, a constellation of six satellites in a sun-synchronous orbit at an altitude of 705 km. The orbit has an inclination of 98.2° with an orbital period of 98.8 minutes and equatorial crossing times at 1:30 p.m. local time on ascending passes and 1:30 a.m. on descending passes. The Atmospheric Infrared Sounder (AIRS) is one of six instruments on board Aqua providing high spatial resolution temperature-sensitive infrared radiances. One AIRS scan consists of 90 individual footprints that cover an across-track distance of 1650 km. The footprint diameter is 13.5 km in the nadir and the along track distance between two scans is 18 km.

The three panels on the top of Fig. 10 show AIRS brightness temperature anomalies, computed from 4.3 micron radiances as described in *Hoffmann and Alexander* [2010]. These are descending orbit swaths with an equatorial crossing time of 1:30 a.m. local time on 5 June 2005 (squall line case), 20 June 2007 (mesoscale convective complex) and 13 June 2013 (mesoscale convective system). In obtaining these images the brightness temperatures of 42 AIRS channels (2322.6 to 2366.9 cm^{-1}) from the 4.3 μm CO_2 ν_3 fundamental band were averaged [*Hoffmann and Alexander*, 2010]. A fourth-order polynomial fit to each cross-track scan has been subtracted to eliminate scan angle dependent brightening effects and other large-scale variations. This procedure removes any waves oriented parallel to the along-track direction. The corresponding mean kernel function computed for midlatitude atmospheric conditions is shown in Fig. 11. It has a broad maximum around 30 to 40 km altitude and a FWHM of 25 km.

The three panels at the bottom of Fig. 10 are computed from idealized model simulations. The size of the idealized model domain is 2000 km ×2000 km. The model is driven with radar-based heating fields that cover the full extent of the model domains. Vertical levels with a constant spacing of 500 m extend from the surface to the bottom of the damping layer, which starts at a height of 50 km. The idealized model runs are initialized at 0000 UTC using one-dimensional wind and temperature profiles computed from MERRA (Modern-era retrospective analysis for research and applications) reanalysis data. Our WRF simulations described in section 2 focused on the time period 0100 UTC to 0800 UTC. The Aqua satellite passes the central United States around 0755 UTC and therefore observes waves that are generated toward the end of this time interval.

The model images in Fig. 10 show the simulated perturbation brightness temperature field at 0755 UTC after applying the kernel function shown in Fig. 11 and mapping the data to a 0.04° latitude-longitude grid. We only use data up to 49 km, the last model level below the damping layer, and consequently only 87.5% of the kernel function is included in our calculation. For the squall line, the MCC, and the MCS case we find that the idealized model accurately reproduces the wave pattern. The match in range of amplitudes is very close for all three cases.

The results presented in this section show that the idealized WRF model forced with a heating field based on radar precipitation rates is able to accurately reproduce the pattern and the amplitudes of observed waves.

6. Conclusion and discussion

We introduced an idealized dry version of the WRF model that is forced with a three-dimensional and time-varying heating/cooling field for wave studies. In conjunction with

the model we developed a heating algorithm to convert local radar precipitation rates into vertical heating/cooling profiles. Focusing on intense convection over the continental summer US this new modeling approach was evaluated by simulating a squall line, a mesoscale convective complex and a mesoscale convective system. We found that radar precipitation data capture the high spatial and temporal variability in occurrence and strength sufficient to define convective sources of gravity waves.

In comparing simulated stratospheric waves to satellite data it was found that both the wave pattern and amplitudes compare well to observations by the AIRS instrument. *Grimsdell et al.* [2010] have presented a similar case study where a dry idealized model was forced with a heating field estimated from scanning-radar measurements. In a comparison to AIRS data they found that their model produced waves that had much smaller amplitude than observed and that good agreement was only achieved when the heating field was multiplied by a factor of 3.8. Our idealized WRF model produces a remarkably high level of realism without further tuning. This advantage can likely be attributed to the method of converting precipitation rates to vertical heating/cooling profiles. In *Grimsdell et al.* [2010] the derivation of the heating field is based purely on thermodynamical arguments. A half sine profile, which is considered representative for convective rainfall [*Shige et al.*, 2004], was chosen for the shape of the vertical heating distribution. The amplitude of the profiles was determined by the column-integrated heating which in turn was calculated from the observed precipitation. This method did not account for advection, ice-phase processes or evaporation. Our heating algorithm is based on the heating profiles generated by a full-physics WRF model and therefore inherently includes these effects. We can

quantify the effects of these processes in our algorithm for comparison to the *Grimsdell et al.* [2010] result. We first examine advection effects.

From the vertical density profile $\rho(z)$ and the vertical distribution of heating/cooling $H(z)$, as given by our algorithm, we can obtain the condensation/evaporation rate $P(z)$ between level z and $z + \delta z$:

$$P(z) = \frac{H(z) C_p \rho(z) \delta z}{\rho_w L_v} \tag{3}$$

Here, C_p denotes the specific heat capacity of air, ρ_w the density of water and L_v the latent heat of condensation/evaporation. The column integrated condensation rate is therefore:

$$P_c = \Sigma_{z=0}^{z=Ztop} P(z), \tag{4}$$

where $Ztop$ denotes the top of the heating profile. The blue line in Fig. 12 shows the ratio of P_c and the surface precipitation P_s, $Rconv = P_c/P_s$ as a function of P_s. Advection causes the surface precipitation rate to be smaller by a factor of 1.5 for small rain rates and by a factor of up to 2.6 for large rain rates. *Shige et al.* [2004] found the same range of values for this quantity.

We next examine the combined effects of advection, ice and evaporation on the maximum heating rate in the profiles. Ice and evaporation primarily affect the shape of the profiles. For a given surface precipitation rate P_s, the quantity R_{G10} is the ratio of the maximum column heating rate in the profile determined by our algorithm and by the method used in *Grimsdell et al.* [2010]. R_{G10} is plotted versus P_s as the red line in Fig. 12. The result shows the maximum heating rate in the profiles given by our algorithm is about three times greater than the maximum resulting from a half-sine shape. These larger heating rates at upper levels in the algorithm profiles are offset by negative con-

tributions at lower levels due to evaporation and melting. Without affecting the surface precipitation rate, they increase the peak of the heating and weight the heating profile toward higher altitudes. Accounting for advection, evaporation and ice-phase processes is therefore necessary to represent gravity-wave generation by convection.

Acknowledgments. The authors would like to thank two anonymous reviewers for their constructive comments to improve the manuscript. We also thank Dr. Lars Hoffmann (email: l.hoffmann@fz-juelich.de) for providing the global 4.3 μm wavenumber-averaged AIRS brightness temperature dataset [*Hoffmann and Alexander*, 2010], which was used to make Figure 10. This work was supported by grant number AGS–1318932 from the National Science Foundation programs in Physical and Dynamic Meteorology and Climate and Large-scale Dynamics. Data used in this study are Next-Generation Radar Level-III products available from the National Oceanic and Atmospheric Administration Satellite and Information Service (http://www.ncdc.noaa.gov/data-access/radar-data) and Atmospheric Infrared Sounder Level 1B radiance sets available from the Goddard Earth Sciences Data and Information Services Center (http://disc.sci.gsfc.nasa.gov/AIRS/). The Weather Research and Forecasting model is a community model supported by the National Center for Atmospheric Research Mesoscale and Microscale Meteorology Division (http://wrf-model.org/index.php).

References

Alexander, M. J. and J. R. Holton (1997), A model study of zonal forcing in the equatorial stratosphere by convectively induced gravity waves, *J. Atmos. Sci.*, *54*, 408–419.

401 Beres, J. H. (2004), Gravity wave generation by a three-dimensional thermal forcing, *J.*
402 *Atmos. Sci.*, *61*, 1805–1815.

403 Beres, J. H., M. J. Alexander and J. R. Holton (2004), A method of specifying the gravity
404 wave spectrum above convection based on latent heating properties and background
405 wind, *J. Atmos. Sci.*, *61*, 324–337.

406 Beres, J. H., R. R. Garcia and B. A. Boville (2005), Implementation of a gravity wave
407 source spectrum parameterization dependent on the properties of convection in the
408 Whole Atmosphere Community Climate Model (WACCM), *J. Geophys. Res.*, *110*,
409 D10108, doi:10.1029/2004JD005504.

410 Braun, S. A. and R. A. Houze Jr. (1996), The heat budget of a midlatitude squall line
411 and implications for potential vorticity production, *J. Atmos. Sci.*, *53*, 1217–1240.

412 Charlton, A. J., A. O'neill, W. A. Lahoz and A. C. Massacand (2004), Sensitivity of
413 tropospheric forecasts to stratospheric initial conditions, *Quart. J. Roy. Meteor. Soc.*,
414 *130*(600), 1771–1792.

415 Choi, H.-J. and H.-Y. Chun (2011), Momentum flux spectrum of convective gravity waves.
416 Part I: An update of a parameterization using mesoscale simulations, *J. Atmos. Sci.*,
417 *68*, 739–759.

418 Chong, M. and D. Hauser (1990), A tropical squall line observed during the COPT 81
419 experiment in west africa. Part III: Heat and moisture budgets, *Mon. Wea. Rev.*, *118*,
420 1696–1706.

421 Chou, M.-D. and M. J. Suarez (1999), A solar radiation parameterization for atmospheric
422 studies, *NASA Tech. Rep.*, *NASA/TM-1999-10460*, 38.

Chun, H.-Y. and J.-J. Baik (2002), An updated parameterization of convectively forced gravity wave drag for use in large-scale models, *J. Atmos. Sci.*, *59*, 1006–1017.

Dee, D. P., S. M. Uppala, A. J. Simmons, P. Berrisford, P. Poli and S. Kobayashi (2011), The ERA-Interim reanalysis: configuration and performance of the data assimilation system, *Quart. J. Roy. Meteor. Soc.*, *137*, 553–597.

Ek, M. B., K. E. Mitchell, Y. Lin, E. Rogers, P. Grummann, V. Koren, G. Gayno and J. D. Tarpley (2003), Implementation of Noah land surface model advances in the National Centers for Environmental Prediction operational mesoscale Eta Model, *J. Geophys. Res.*, *108*, D20111, doi:10.1029/2002JD003296.

Grimsdell, A. W., M. J. Alexander, P. T. May and L. Hoffmann (2010), Model study of waves generated by convection with direct validation via satellite, *J. Atmos. Sci.*, *5*, 1617–1631.

Hoffmann, L. and M. J. Alexander (2010), Occurrence frequency of convective gravity waves during the North American thunderstorm season, *J. Geophys. Res.*, *115*, doi: 10.1029/2010JD014401.

Hong, S.-Y., Y. Noh and J. Dudhia (2006), A new vertical diffusion package with an explicit treatment of entrainment processes, *Mon. Wea. Rev.*, *109*, 1–21.

Hoskins, B. J. (1983), Dynamical processes in the atmosphere and the use of models, *Quart. J. Roy. Meteor. Soc.*, *118*, 819–850.

Kain, J. S. and J. M. Fritsch (1990), A one-dimensional entraining detraining plume model and its application in convective parameterization, *J. Atmos. Sci.*, *47*, 2784–2802.

Kim, Y.-H., A. C. Bushell, D. R. Jackson and H.-Y. Chun (2013), Impacts of introducing a convective gravity-wave parameterization upon the QBO in the Met Office Unified

Model, *Geophys. Res. Lett*, *40*, doi:10.1002/grl.50353.

Knievel, J. C., G. H. Bryan, and J. P. Hacker, 2007: Explicit numerical diffusion in the WRF model, *Mon. Wea. Rev.*, *135*, 3808–3824.

Lane, T. P., M. J. Reeder and T. L. Clark (2001), Numerical modeling of gravity wave generation by deep tropical convection, *J. Atmos. Sci.*, *58*, 1249–1274.

Manzini, E., A. Yu. Karpechko, J. Anstey, M. P. Baldwin, R. X. Black, C. Cagnazzo, N. Calvo, A. Charlton-Perez, B. Christiansen, P. Davini, E. Gerber, M. Giorgetta, L. Gray, S. C. Hardiman, Y.-Y Lee, D. R. Marsh, B. A. McDaniel, A. Purich, A. A. Scaife, D. Shindell, S.-W. Son, S. Watanabe and G. Zappa (2014), Northern winter climate change: Assessment of uncertainty in CMIP5 projections related to stratosphere-troposphere coupling, *J. Geophys. Res. Atmos.*, *119*, 7979–7998, doi: 10.1002/2013JD021403.

Mlawer, E. J., S. J. Taubman, P. D. Brown, M. J. Iacono and S. A. Clough (1997), Radiative transfer for inhomogeneous atmospheres: RRTM, a validated correlated-k model for the longwave, *J. Geophys. Res.*, *102*, 16663–16682.

Moncrieff, M. W. (1992), Organized mesoscale convective systems: Archetypal dynamical models, mass and momentum flux theory and parametrization, *Quart. J. Roy. Meteor. Soc.*, *118*, 819–850.

Morrison, H., G. Thompson and V. Tatarskii (2009), Impact of cloud microphysics on the development of trailing stratiform precipitation in a simulated squall line: Comparison of one- and two-moment schemes, *Mon. Wea. Rev.*, *137*, 991–1007.

Morrison, H. and J. Milbrandt (2011), Comparison of two-moment bulk microphysics schemes in idealized supercell thunderstorm simulations, *Mon. Wea. Rev.*, *139*, 1103–

1130.

Pawson, S. et al. (2000), The GCM-reality intercomparison project for SPARC (GRIPS): scientific issues and initial results, *Bulletin Am. Meteorol. Soc.*, *81*, 781–796.

Piani, C., D. Durran, M. J. Alexander and J. R. Holton (2000), A numerical study of three-dimensional gravity waves triggered by deep tropical convection and their role in the dynamics of the QBO, *J. Atmos. Sci.*, *57*, 3689–3702.

Roff, G., D. W. J. Thompson and H. Hendon (2011), Does increasing model stratospheric resolution improve extended-range forecast skill?, *Geophys. Res. Lett*, *38*(5), doi:10.1029/2010GL046515.

Rotunno, R., J. B. Klemp and M. L. Weisman (1988), A theory for strong long-lived squall lines, *J. Atmos. Sci.*, *45*, 463–485.

Sato, K., S. Watanabe, Y. Kawatani, Y. Tomikawa, K. Miyazaki and M. Takahashi (2009), On the origins of mesospheric gravity waves, *Geophys. Res. Lett*, *36*(19), doi: 10.1029/2009GL039908.

Sato, K., S. Tateno, S. Watanabe and Y. Kawatani (2012), Gravity wave characteristics in the southern hemisphere revealed by a high-resolution middle-atmosphere general circulation model, *J. Atmos. Sci.*, *69*, 1378–1396.

Scaife, A. A., T. Spangehl, D. R. Fereday, U. Cubasch, U. Langematz, H. Akiyoshi, S. Bekki, P. Braesicke, N. Butchart, M. P. Chipperfield, A. Gettelman, S. C. Hardiman, M. Michou, E. Rozanov and T. G. Shepherd (2011), Climate change projections and stratosphere-troposphere interaction, *Climate Dyn.*, doi:10.1007/s00382-011-1080-7.

Schirber, S., E. Manzini, T. Krismer and M. Giorgetta (2014), The quasi-biennial oscillation in a warmer climate: sensitivity to different gravity wave parameterizations.

Climate Dyn., doi:10.1007/s00382-014-2314-2

Shige, S., Y. N. Takayabu, W.-K. Tao and D. E. Johnson (2004), Spectral retrieval of latent heating profiles from TRMM PR data. Part I: Development of a model-based algorithm, *J. Appl. Meteor.*, *43*, 1095–1113.

Skamarock, W. C. (2004), Evaluating mesoscale NWP models using kinetic energy spectra, *Mon. Wea. Rev.*, *132*, 3019–3032.

Skamarock, W., J. B. Klemp, J. Dudhia et al. (2008). A Description of the Advanced Research WRF Version 3, NCAR Technical Note NCAR/TN-475+STR, doi: 10.5065/D68S4MVH

Song, I.-S., H.-Y. Chun and T. P. Lane (2003), Generation mechanisms of convectively forced internal gravity waves and their propagation to the stratosphere, *J. Atmos. Sci.*, *60*, 1960–1980.

Song, I.-S. and H.-Y. Chun (2008), A Lagrangian spectral parameterization of gravity wave drag induced by cumulus convection, *J. Atmos. Sci.*, *65*, 1204–1224.

Stephan, C. C. and M. J. Alexander (2014), Summer season squall line simulations: Sensitivity of gravity waves to physics parameterization and implications for their parameterization in global climate models, *J. Atmos. Sci.*, *71*(9), 3376–3391.

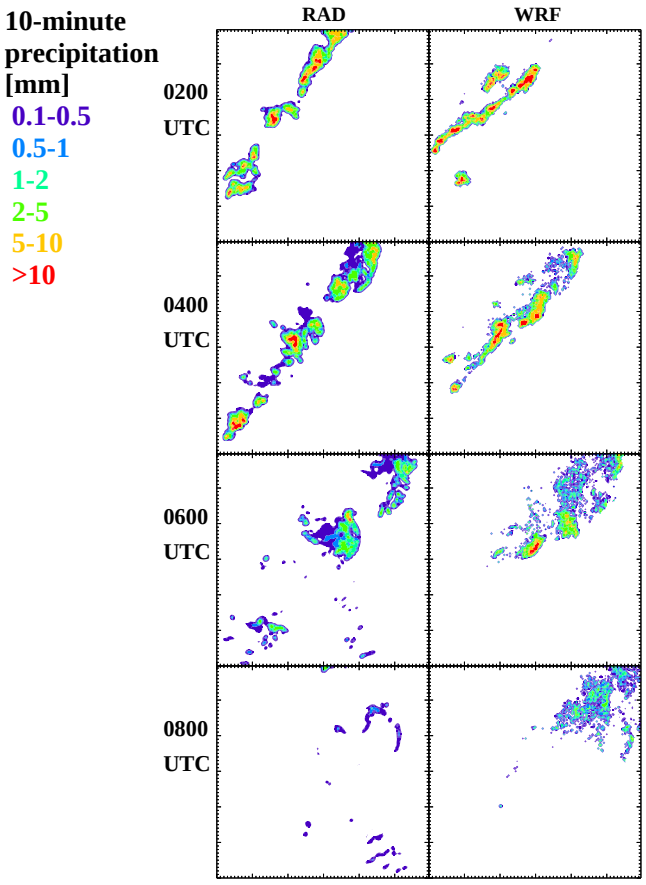

Figure 1. Maps of measured (RAD) and simulated (WRF) precipitation for the squall line case. Each panel shows the ten-minute accumulated precipitation over the area of the innermost model domain spanning 600 km ×600 km. Rows are labeled with the hour in UTC. The left column contains radar measurements and the right column displays simulated values. All plots are based on a horizontal resolution of 4 km.

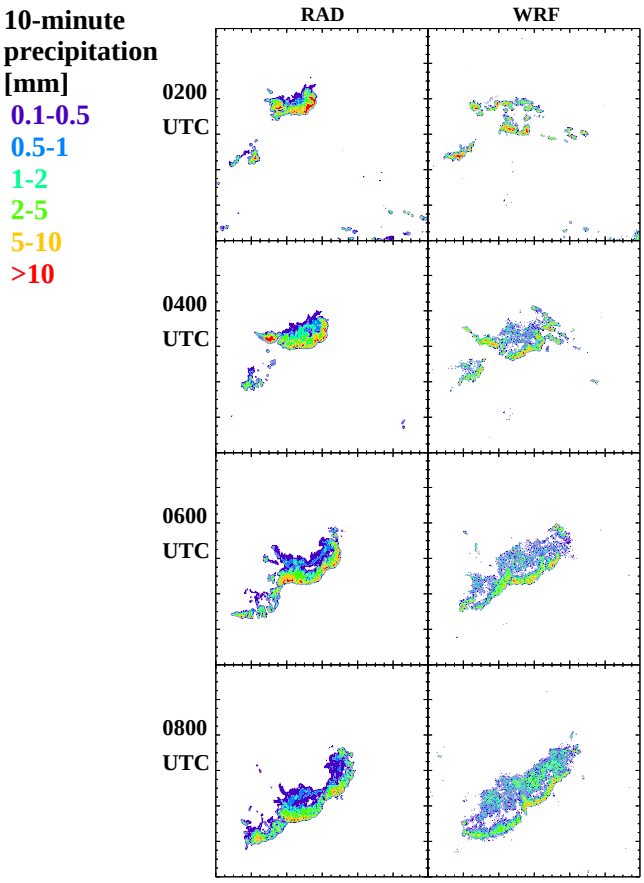

Figure 2. Maps of measured (RAD) and simulated (WRF) precipitation for the mesoscale convective complex. Each panel shows the ten-minute accumulated precipitation over the area of the innermost model domain spanning 1200 km ×1200 km. Rows are labeled with the hour in UTC. The left column contains radar measurements and the right column displays simulated values. All plots are based on a horizontal resolution of 4 km.

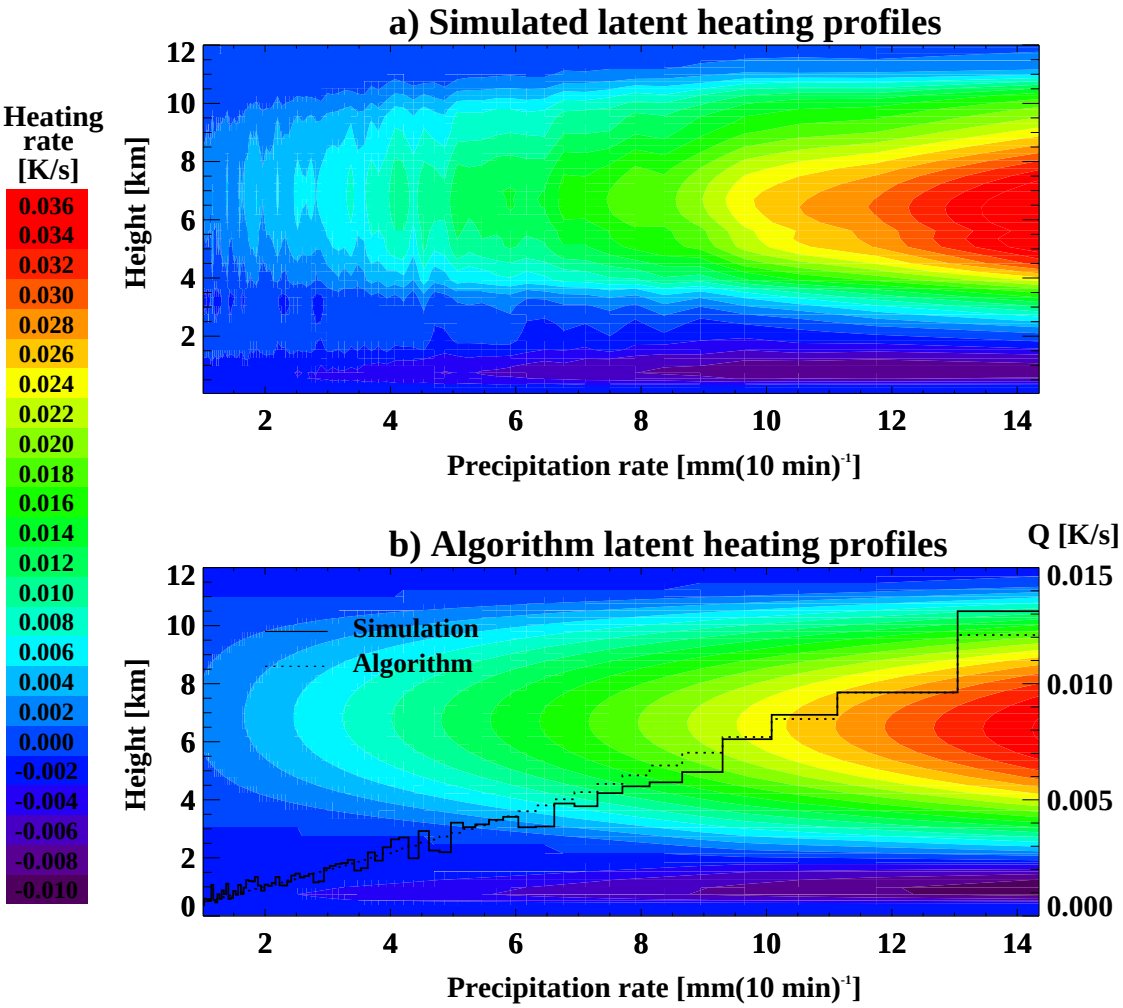

Figure 3. Simulated (a) and algorithm-derived (b) latent heating/cooling profiles versus precipitation rate. These are averages of convective pixels in the 600 km ×600 km domain based on a horizontal resolution of 4 km ×4 km and ten-minute time intervals between 0100 UTC and 0800 UTC. The histograms in panel b pertain to the ordinate on the right hand side and show the density-weighted vertically integrated heating rates, labeled Q. Dashed lines are for the algorithm-generated profiles and solid lines for the simulated profiles.

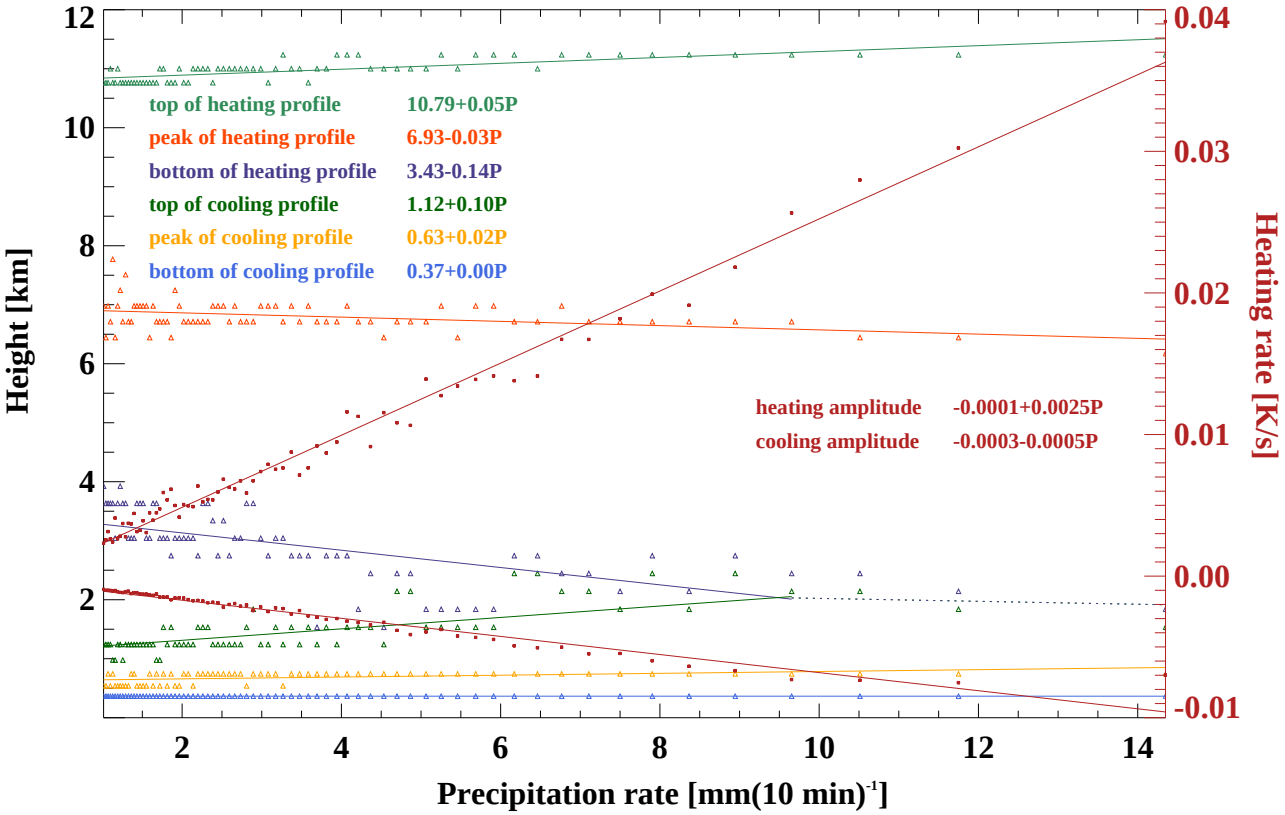

Figure 4. Linear relationships describing key characteristics of the algorithm for vertical heating profiles and their dependence on ten-minute precipitation rate. Individual data points are derived from convective rain pixels in the squall line simulation and lines are linear fits. Light green: top of the heating, Orange: height of maximum heating rate, Purple: bottom of the heating profile, Dark green: top of the cooling region, Yellow: height of maximum cooling, Blue: bottom of cooling profile. The dark red data points pertain to the ordinate on the right-hand side and show the heating and cooling layer amplitudes. These linear fits are used to convert ten-minute precipitation rates to vertical heating profiles. All values are based on a resolution of 4 km ×4 km and the time interval 0100 UTC to 0800 UTC.

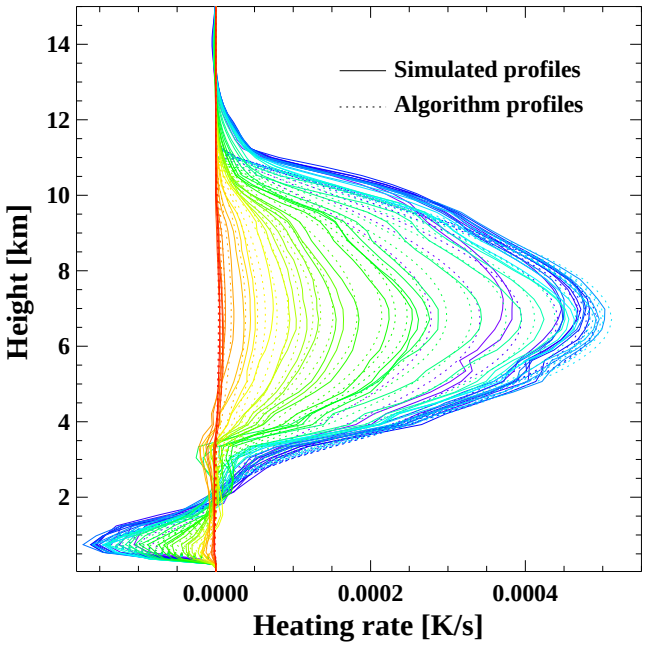

Figure 5. Simulated (solid lines) and the algorithm-produced (dashed lines) vertical heating profiles every ten minutes between 0100 UTC and 0800 UTC. Blue to red colors indicate increasing times. Each profile is a domain average of convective columns as defined in the text.

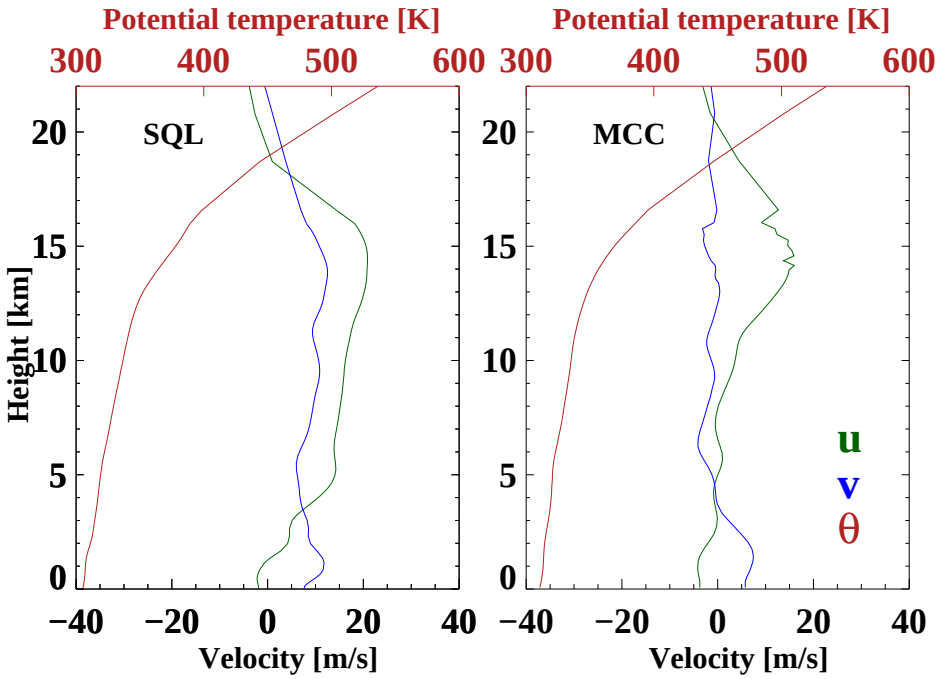

Figure 6. Zonal wind (green), meridional wind (blue) and potential temperature (red) soundings used to initialize the idealized model for the squall line (SQL) and the mesoscale convective complex (MCC) simulation. The profiles are calculated from the domain-mean 0100 UTC wind and temperature fields of the respective full-physics simulations.

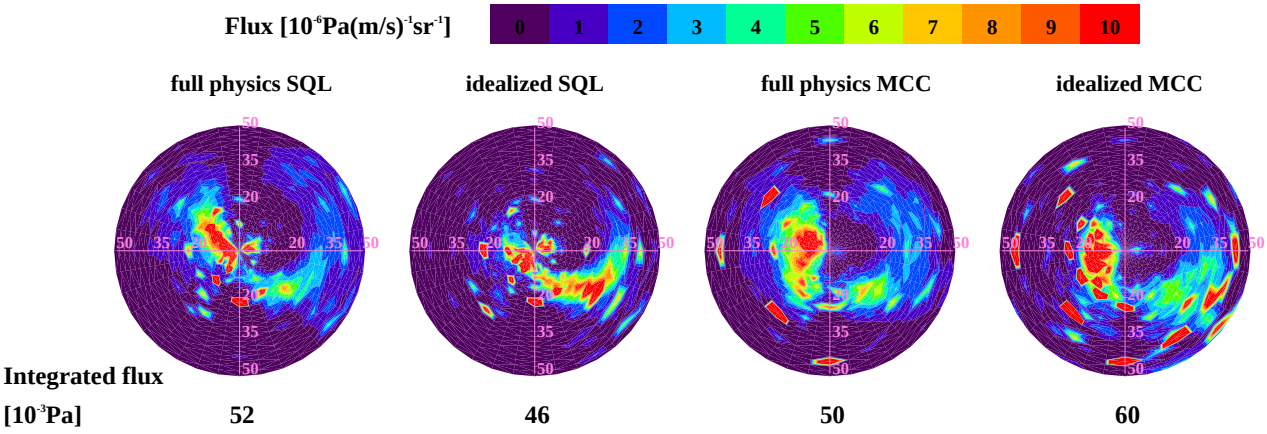

Figure 7. Gravity wave momentum flux spectra at 95 hPa for the squall line (SQL) and mesoscale convective complex (MCC) simulations. The idealized model is driven by a heating/cooling field derived from the precipitation field of the corresponding full-physics simulation. The radial coordinate with a resolution of 2 m/s is phase speed and the angular coordinate with a resolution of 10° denotes propagation direction. Northward is at the top and eastward right in each plot. The numbers below the plot denote the total flux integrated over all phase speeds and propagation angles.

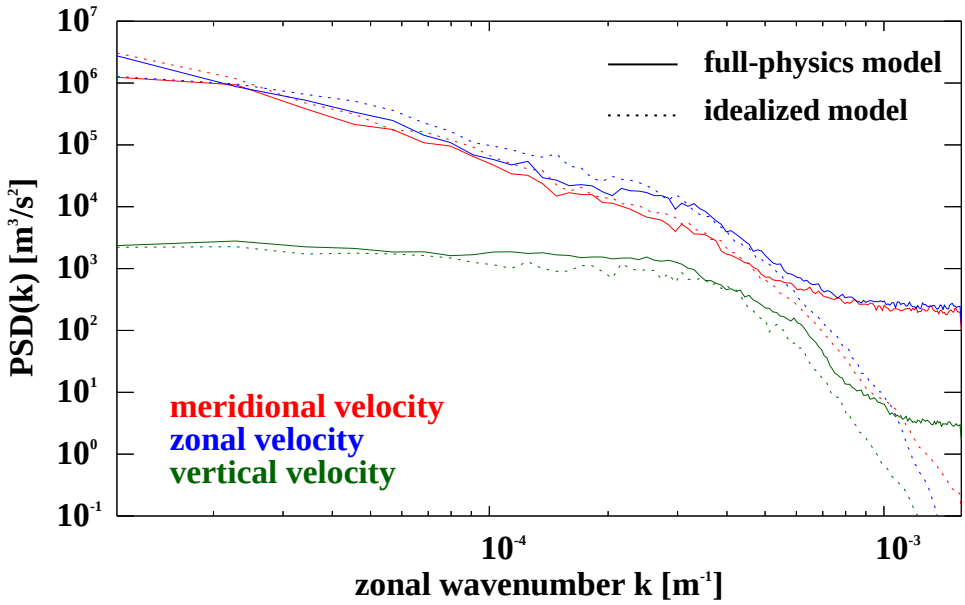

Figure 8. Power spectral density as a function of horizontal wavenumber for the zonal (blue), meridional (red) and vertical (green) velocity components at 95 hPa and 0500 UTC for the squall line case. Dashed curves are for the idealized model and solid curves for the full-physics model. The spectra of both models start to decay around $4{\cdot}10^{-4}\mathrm{m}^{-1}$, which corresponds to a horizontal wavelength of about 16 km or 8 times the grid scale and is consistent with the WRF model's effective resolution of about $7\Delta x$ [*Skamarock*, 2004].

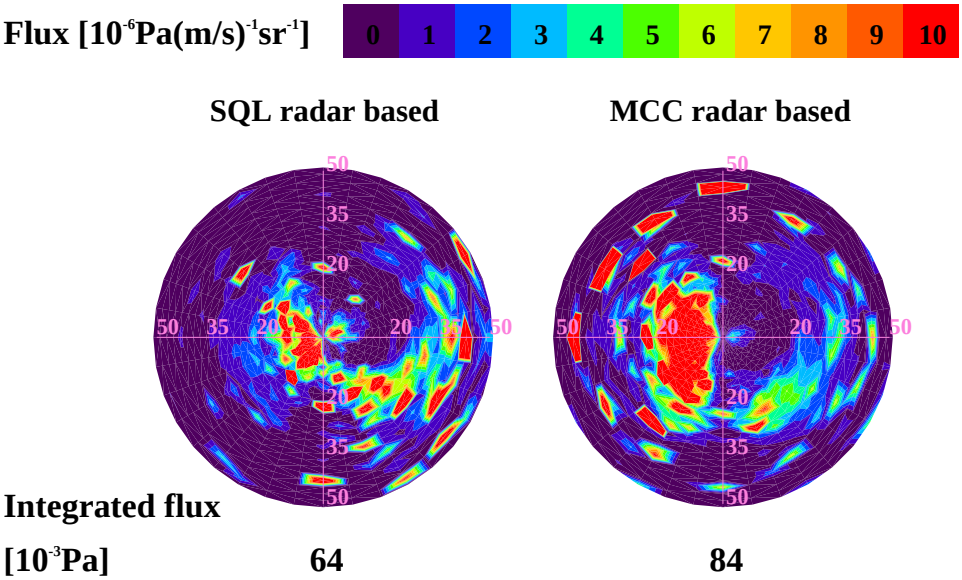

Figure 9. Gravity wave momentum flux spectra at 95 hPa for the idealized squall line (SQL) and mesoscale convective complex (MCC) simulations based on radar data. For these simulations the heating/cooling field is directly derived from ten-minute radar precipitation fields. As in Fig. 7 the radial coordinate with a resolution of 2 m/s is phase speed and the angular coordinate with a resolution of 10° denotes propagation direction. Northward is at the top and eastward right in each plot. The numbers below the plot denote the total flux integrated over all phase speeds and propagation angles.

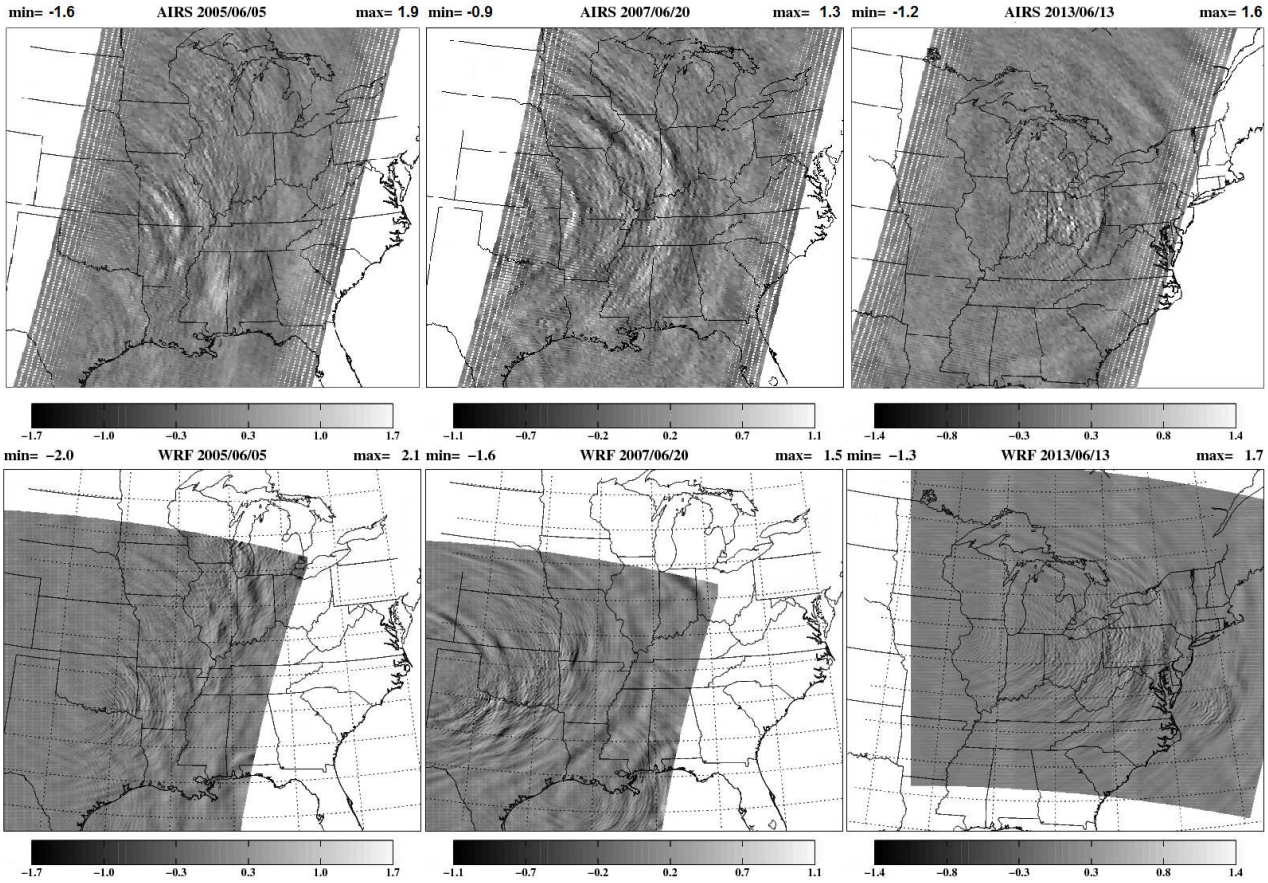

Figure 10. The top panels show AIRS brightness temperature anomalies. These are descending orbit swaths with an equatorial crossing time of 1:30 am local time on 5 June 2005 (squall line case), 20 June 2007 (mesoscale convective complex) and 13 June 2013 (mesoscale convective system). A fourth-order polynomial fit along the across-track direction has been subtracted. The images on the bottom are computed from the idealized model driven with a radar-precipitation-derived heating. Shading denotes temperature anomalies in Kelvin at the same time as the satellite measurements. Each panel is also labeled with maximum and minimum values in the wave field.

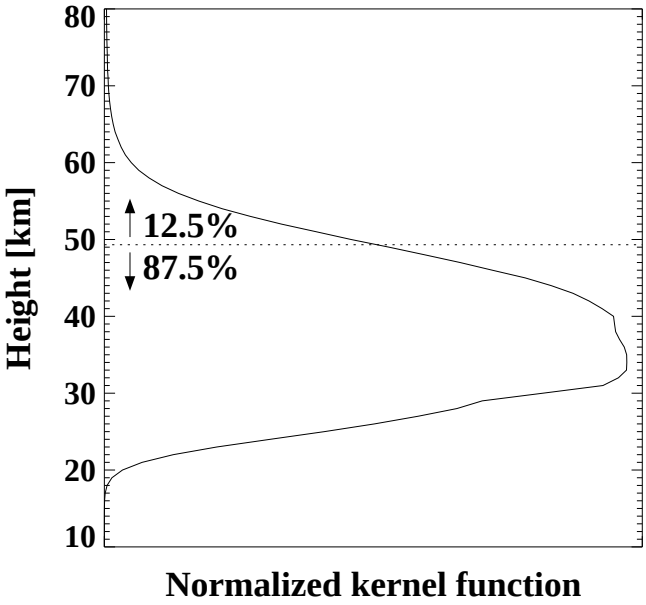

Figure 11. Normalized mean kernel function for 42 AIRS channels (2322.6-2366.9 cm^{-1}) in the 4.3 μm CO_2 band. The dashed line indicates the height of the last model level situated below the damping layer. The contribution of levels below 49 km (i.e. levels that are included in our calculation) to the kernel function is 87.5%.

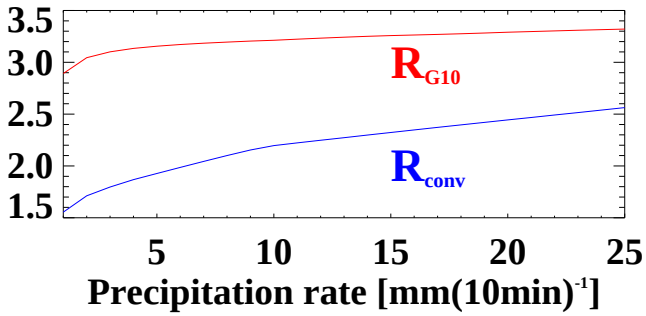

Figure 12. The quantity $Rconv = P_c/P_s$ (blue line) is defined as the ratio of the vertically integrated column condensation/evaporation rate and the surface precipitation rate. $Rconv$ is larger than one because hydrometeors are transported out of the column. The quantity R_{G10} (red line) is the ratio of the maximum column heating rate in the profile derived by our algorithm and the method used in *Grimsdell et al.* [2010]. Our algorithm is based on a full-physics model and accounts for ice-phase processes and evaporation while the Grimsdell method neglected these processes. The top of the heating is assumed to be identical in both.